Published in final edited form as:
Neurosurgery. 2008 October ; 63(4): 782–789. doi:10.1227/01.NEU.0000325490.80694.A2.

ADVANCED MAGNETIC RESONANCE IMAGING OF CEREBRAL CAVERNOUS MALFORMATIONS: I. HIGH FIELD IMAGING OF EXCISED HUMAN LESIONS

Robert Shenkar, PhD[1], **Palamadai N. Venkatasubramanian, PhD**[2], **Jin-cheng Zhao, MD**[1], **H. Hunt Batjer, MD**[1], **Alice M. Wyrwicz, PhD**[2,3], and **Issam A. Awad, MD**[1]

1 *Division of Neurosurgery, Department of Neurological Surgery, Feinberg School of Medicine, Northwestern University, Chicago, Illinois*

2 *Center for Basic MR Research, Evanston Northwestern Healthcare, Department of Radiology, Feinberg School of Medicine, Northwestern University, Chicago, Illinois*

3 *Department of Anesthesiology, Feinberg School of Medicine, Northwestern University, Chicago, Illinois*

Abstract

Objectives—We hypothesized that structural details would be revealed in cerebral cavernous malformations (CCMs) through the use of high field magnetic resonance (MR) and confocal microscopy, which have not been described previously. The structural details of CCMs excised from human patients were sought by examination with high field MR imaging, and correlated with confocal microscopy of the same specimens. Novel features of CCM structure are outlined, including methodological limitations, venues for future research and possible clinical implications.

Methods—CCM lesions excised from four patients were fixed in 2% paraformaldehyde and subjected to high resolution MR imaging at 9.4 or 14.1 Tesla by spin-echo and gradient recalled echo methods. Histological validation of angioarchitecture was conducted on thick sections of CCM lesions using fluorescent probes to endothelium under confocal microscopy.

Results—Images of excised human CCM lesions were acquired with proton density-weighted, T_1-weighted, T_2-weighted spin echo and T_2*-weighted gradient-recalled echo MR. These images revealed large “bland” regions with thin walled caverns, and “honeycombed” regions with notable capillary proliferation and smaller caverns surrounding larger caverns. Proliferating capillaries and caverns of various sizes were also associated with the wall of apparent larger blood vessels in the lesions. Similar features were confirmed within thick sections of CCMs by confocal microscopy. MR relaxation times in different regions of interest suggested the presence of different states of blood breakdown products in areas with apparent angiogenic proliferative activity.

Conclusions—The high field MR imaging techniques demonstrate novel features of CCM angioarchitecture, visible at near histological resolution, including regions with apparently different biologic activity. These preliminary observations will motivate future research, correlating lesion biologic and clinical activity with features of MR imaging at higher field strength.

Corresponding Author Information Page: Address for correspondence and reprints: Robert Shenkar, PhD, Evanston Northwestern Healthcare, Division of Neurosurgery, 2650 Ridge Avenue Room 4222, Evanston, IL 60201, Fax number: 847-733-5256, Telephone number: 847-570-2177, Email: rshenkar@enh.org.

Financial Disclosures: None of the authors received any financial support in conjunction with the generation of their submission.

Keywords

imaging/intracranial hemorrhage/MRI/stroke; hemorrhagic/vascular malformations

Introduction

The cerebral cavernous malformation (CCM) is a highly prevalent vascular lesion in the human brain, affecting more than 1 million Americans, and predisposing them to a lifetime risk of stroke and epilepsy (16,19,22–24). The lesions consist of clusters of cavernous anomalous vessels, lined by endothelium, and filled with blood at various stages of thrombosis (6,8,10, 33). They invariably exhibit hallmarks of blood leakage and gliotic reaction in adjacent brain. The CCMs appear to grow by a process of cavern proliferation in the setting of repetitive lesional hemorrhages (hemorrhagic proliferative dysangiogenesis), and exhibit brittle vascular morphology devoid of mature vessel wall elements (12,24,26). It is not known if caverns arise from other caverns, novel capillaries or pre-existing blood vessels.

The CCM lesions were thought to be rare, until the advent of imaging by magnetic resonance (MR). Conventional MR sequences (T_1- and T_2-weighted imaging) are capable of visualizing clinically significant CCM lesions with specificity and sensitivity approaching 100% (21), while in familial cases (13), gradient echo MR sequences may reveal a larger number of smaller occult lesions (15). These MR scans can also accurately document gross lesion hemorrhage and expansion (9,34). However, the majority of CCM lesions remain apparently clinically and biologically quiescent during most of the host's lifetime, except for phases of possible proliferation and clinically overt hemorrhage. The spatial resolution necessary to visualize the angioarchitecture and proliferative activity of CCMs remain quite limited in MR imaging at lower field strengths available clinically at the present time.

The objectives for this study are to image human CCM lesions *ex vivo* at high magnetic field, with correlative confocal microscopy and to outline potential pathobiologic significance of these observations, with venues for future research and possible clinical implications. We also evaluated whether magnetic susceptibility artifacts at higher field strengths enhance or degrade details of MR imaging of CCM lesions. We hypothesized that high field imaging with greater spatial resolution can reveal more details of the structure of CCMs than those seen in clinical images at lower field strength.

Subjects and Methods

CCM Specimen

CCM specimen were obtained during surgery at Evanston Northwestern Healthcare (ENH), Northwestern Memorial Hospital and the University of Virginia Hospital from patients (n = 4) diagnosed previously by clinical MR imaging at 1.5 Tesla (T). The subjects (one male and three females) were 23 to 59 years of age. Two subjects had recent hemorrhages from the CCM within three months before surgery; two subjects had clinically quiescent lesions. One subject harbored multiple lesions; three subjects had single lesions. Three subjects experienced seizure disorders. All CCM lesions, ranging in size from 10 to 50 mm, were located supratentorially. This study was approved by the ENH Institutional Review Board. All subjects gave informed consent. After surgical removal of the CCMs, lesions were rinsed in saline and immersed in 2% paraformaldehyde for two to four weeks before imaging.

MR Imaging

Immediately before MR imaging, the excised fixed CCM specimens were rinsed with phosphate buffered saline (PBS) and placed securely into glass vials immersed were in Fomblin Y LVAC 06/6 perfluoropolyether (Sigma-Aldrich, St. Louis, MO) during imaging. Fomblin is an inert liquid which is commonly used in MR microimaging to prevent dehydration and reduce magnetic susceptibility gradients. It does not alter any tissue characteristics (14). High spatial resolution MR images were acquired on a 9.4 T Bruker vertical axis imager (400 MHz proton frequency) or a 14.1 T Bruker Avance imaging spectrometer (600 MHz proton frequency), using a 20-mm volume resonator tuned to the appropriate proton frequency. Two-dimensional multi-slice spin-echo images were acquired using the following repetition time/echo time (TR/TE): Proton density-weighted imaging –2000ms/10ms, T_1-weighted imaging -400ms/10ms and T_2-weighted imaging - 4000ms/40ms. Gradient-recalled echo images were acquired using TR/TE 50–500ms/4–10ms. Slice thickness was 100 – 200 μm and in-plane pixel size was 35 – 40 μm. Three-dimensional gradient-recalled echo images were acquired using TR/TE 50–200msec/4msec and 60–90μm isotropic pixel size.

Confocal Microscopy

After MR imaging, the tissue was rinsed in PBS and immersed into 2% paraformaldehyde. The crosslinks were reversed in 0.01 mol/L citrate buffer pH 6.0, 95°C for 25 minutes. The tissue was cut into 200-μm sections with a Vibratome Model G sectioning system (Oxford Laboratories, Foster, CA). The thick sections were placed on microscope slides, blocked with goat IgG antibody (Santa Cruz Biotechnologies, Santa Cruz, CA) at 1:20 dilution for one hour, treated with Image-iT FX signal enhancer (Molecular Probes, Eugene, OR). To stain endothelium, the specimen was incubated overnight with streptavidin-alexa-568 (Molecular Probes) at 1 μg/μl or with rabbit anti-human von Willebrand factor (Sigma-Aldrich, St. Louis, MO) at 1:300 dilution followed by incubation for 1 hour with goat anti-rabbit-Alexa-568 (Molecular Probes) at 1:300 dilution. It was then incubated with 70% ethanol for 2 minutes, treated with 2% Sudan Black-B in 70% ethanol for 3 minutes, incubated with 70% ethanol for 1 minute and rinsed twice in deionized water for 3 minutes. Coverslips were mounted with Prolong Gold antifade reagent (Molecular Probes). A D-eclipse C1 confocal microscope (Nikon Instruments Inc., Melville, NY) was used to view the sections using a 543 nm helium neon laser.

MR Relaxation Times

T_1 and T_2 relaxation times were measured simultaneously in each pixel of an image from one slice of a human CCM using progressive saturation (11) and CPMG (Carr-Purcell-Meiboom-Gill) (7,17) methods, respectively. T_2* was measured in a human CCM specimen at 14.1 T by varying echo delay time at constant recycle time in a gradient-recalled echo imaging sequence.

Results

T_1-weighted (TR/TE 550ms/10ms) and T_2-weighted (TR/TE 3700ms/100ms) brain images of a patient acquired prior to surgery on a 1.5 T clinical MR scanner are presented in Figure 1. These clinical images, however, do not reveal finer angioarchitectural or structural features within the lesion. High field MR images of the lesion from the same patient were acquired *ex vivo* on a 9.4 T micro-imager with different imaging sequences. In contrast to the low spatial resolution clinical images, the proton density weighted images (Figure 1C), and the T_1-weighted images (Figure 1D), acquired at high field strength, with high spatial resolution reveal the caverns comprising the lesion, reflecting histopathologic CCM appearance. Furthermore, these images reveal a markedly heterogeneous microstructure within the specimen. Large caverns, greater than 500 om in diameter and present at various locations within the lesion, represent the most striking feature of the CCM image. Besides these caverns, numerous smaller

hypointense spots of varying sizes less than 100 om in diameter are seen throughout the landscape in each image. The T_2- (Figure 1E) and T_2*- (Figure 1F) weighted images are largely hypointense with a small hyperintense patch in each image. The observed variations in endogenous contrasts generated with T_1-, T_2-, and T_2*-weighted imaging indicates that the CCM lesion contains iron in different breakdown products of hemoglobin (4).

The proton density-weighted image (Figure 1C) was enlarged (Figure 2A) to show more detail. After MR imaging, part of the lesion (within the square depicted in Figure 2A) was cut into 200-μm thick sections for correlative confocal microscopy. Both the MR (Figure 2A) and confocal (Figure 2B) images gave a three-dimensional perspective of the angioarchitecture of the CCM lesion. These images both showed small caverns with diameters < 100 μm (arrows) surrounding larger caverns, and along an apparent blood vessel, i.e. a tubular structure confirmed on three dimensional reconstruction of MR images, and by confocal microscopy, in contrast to bubble like dilated caverns and smaller capillaries.

High field MR images for each of the CCM lesions revealed both “bland” and “honeycombed” regions. We define “bland” regions as hyperintense areas with larger caverns (0.5 – 1 mm) devoid of other details, and “honeycombed” regions as hypointense areas with smaller caverns or capillaries (< 100 μm in diameter) proliferating around larger caverns and apparent blood vessels (arrows). Figure 3 illustrates these features in three dimensional gradient-recalled echo T_2*-weighted MR images obtained at 14.1 T of one such lesion. All four CCM specimens examined had a predominance of “bland” over “honeycombed” features. Confocal microscopy confirmed the presence of similar features (Figure 4B and D) as identified by reconstructed high resolution MR imaging at 9.4 T or 14.1 T (Figures 4A and C).

We measured T_1 and T_2 relaxation times in the CCM specimen from one case at 14.1 T and demonstrated regional differences in relaxation times within the specimen. Regional relaxation times were calculated by averaging T_1 or T_2 for all the pixels in the regions of interest (ROIs) shown in Figure 5 and are presented in Table 1. There appears to be two distinct regions in this specimen, one characterized by T_1 relaxation time > 1 sec and the other < 1 sec. Notably, all four “honeycombed” areas (ROIs 1–4) have larger T_1 and T_2 relaxation times than the five “bland” regions (ROIs 5–9). The average T_1 of the ROIs with the larger T_1 is 1.55 sec. The average T_1 of the ROIs with the shorter T_1 is 0.40 sec. The larger T_1 ROIs have an average T_2 of 29 msec, while the shorter T_1 ROIs have a shorter T_2 average of 14.7 msec.

T_2* relaxation times varied between 8.0 and 19.1 msec in different regions of the sample. There were large standard deviations of T_2* relaxation times measurements in regions with “honeycombed” appearance, limiting the accuracy of those measurements in those regions. The observed regional differences in T_1, T_2 and T_2* relaxation times suggest the presence of iron in different oxidation states, in different breakdown products and perhaps in different amounts in the angioarchitectural features seen in human CCM.

Discussion

The results described in the present study supported the hypothesis that high field MR imaging reveals structural details in CCMs that have not been described previously. The three dimensional angioarchitecture of caverns was illustrated and the spatial organization within the lesions was preserved despite the high magnetic field. Novel structural features included small caverns surrounding larger caverns and arranged on tubular structures that resemble mature blood vessels coursing through the lesions. These features may have implications in the diagnostic evaluation of CCM disease, and its correlation with clinical behavior and therapeutic manipulation.

Regional Heterogeneity of MR Relaxation Times in CCM Lesions

Conventional histologic features of CCM lesions have been traditionally examined using formalin-fixed paraffin-embedded specimens cut to only a few micrometers thick, with immunohistochemical and other staining of relevant molecular markers in cross sections of the caverns, intercavernous matrix, and associated capillary proliferation (25,27,30–32). Such studies have revealed evidence of proliferative angiogenesis in the lesions and a number of differential structural and functional features of CCMs in comparison to control vessels (25, 27,30–32). Electron microscopy has allowed a more detailed examination of ultrastructural pathology of the endothelial layer and basement membrane (29,33). Due to the thinness of these sections, only cross sections of caverns and blood vessels of various sizes could be described, without revealing three-dimensional connections between these structures, nor the state of iron breakdown products in various regions of the lesion.

Conversely, conventional MR imaging at low field strength (≤ 3 T) has revealed larger cavernous structures (> 1 mm in diameter), and mixed signal from blood breakdown products within CCM lesions, but not their detailed angioarchitecture. In the present investigation, we examine high field MR images at near histologic resolution and confocal microscopic images of slices that are on the order of hundreds of micrometers thick. The immunohistochemical fluorescence of endothelial cells by confocal microscopy allowed the visualization of complex capillary and cavern angioarchitecture in correlation with MR images. This provided an integrated picture of histologic and three-dimensional anatomy in a way not possible from conventional thin section cross sectional slides.

Before surgery, brain images were acquired with clinical MR imagers at 1.5 T or 3 T field strengths. Although the resolution was low, the T_1-weighted brain images suggested the presence of caverns of various sizes. In addition, T_2-weighted images revealed signal of blood breakdown products of apparently different ages within the lesion, and more chronic, likely hemosiderin, hypointense stain around the lesion. These findings have been described previously (2,20). *Ex vivo* images of CCM specimens that were acquired by high field strength MR at 9.4 T or 14.1 T with different relaxation sequences illustrated various endogenous contrasts within the lesions. Several caverns greater than 500 μm in diameter and a linear structure that might be a blood vessel appear hypointense on the T_1–weighted image and are very dark on the T_2-weighted image. This is consistent with the possibility that these structures contain deoxyhemoglobin and/or hemosiderin, which have previously been shown to be slightly hypointense on T_1–weighted images and very hypointense on T_2–weighted images (4). A bright region in the T_2-weighted image also appears to be brighter than background in the proton density and T_1–weighted images. This region possibly contains extracellular methemoglobin, which has previously been shown to be hyperintense on both T_1–weighted images and on T_2–weighted images (4).

T_1 and T_2 relaxation times varied in different regions of the CCM lesions suggesting that iron is present in various degradation products of hemorrhage in specific regions of the lesion. These include mainly hemosiderin, which because of high magnetic susceptibility, appears very hypointense in T_2-weighted images (2,4). The relaxation times recorded herein may not apply to fresh specimen, or to lesions *in vivo*. Other studies have demonstrated a reduction in proton density, T_1 and T_2 signals over time during brains were fixed in formalin (3,28,35). However, the measurements will serve as a basis for comparison among specimens under similar conditions and between different regions within the same specimen, and for future studies defining the biophysical nature of the signal heterogeneity within and among lesions.

Bland versus Honeycombed Regions

The present work describes two types of angioarchitectural features within the CCM lesions that have not been previously reported. There appear to be “bland” caverns of various sizes, unassociated with capillary or small cavern proliferation. Other more hypointense regions include “honeycombed” feature, with small caverns or dilated capillaries apparently surrounding a larger cavern or an apparent blood vessel.

Potential Clinical Implications and Areas of Future Research

Clinical imaging may become possible *in vivo* at higher field strengths. A recent report has shown the same level of details in clinical MR imaging at 8 T of a patient with proliferative capillary telangiectasia, likely representing an early stage of CCM genesis (18). The same features of lesion angioarchitecture revealed at high field imaging may be definable by optimized sequences at medium field strengths (3–6 T) likely to be more widely available clinically in upcoming years. Higher field imaging may reveal other features of lesion phenotype in sporadic versus familial lesions, and in lesions associated with previous brain irradiation, venous developmental anomaly, or different familial genetic substrates. These same features of lesion behavior will need to be sought and followed over time, in correlation with clinical lesion activity. The number of cases in our preliminary studies was too small and the sampling bias of imaging too great for meaningful correlation with recent clinical behavior.

Most CCM lesions remain clinically quiescent in the host’s lifetime, except for brief periods of apparent proliferation and hemorrhage. It will be useful to define biologic states underlying clinical activity in these lesions. The preliminary correlations with confocal immunomicroscopy of thick sections of the same lesions allowed confirmation of broad angioarchitectural features. But the technical difficulties of working with thick sections of fresh tissue prevented more detailed biologic correlations. Further technical optimization of correlative imaging will be needed, including dual probes for MR and fluorescent labeling of the same cells. New T_1 contrast agents that contain chelated gadolinium and a fluorophore along a polymer background conjugated to specific antibodies against markers for endothelium and inflammatory cells, being developed in a collaborating laboratory at our institution (T. Meade, unpublished data), would provide a platform for the development and validation of molecular imaging (5) giving another dimension for validating molecular profiles in different regions of these lesions, hopefully reflecting aggressive and quiescent states and clinical behavior of CCMs.

In future work with CCM lesions surgically excised from human patients or within the brains of murine models *in vivo*, we are hypothesizing that inflammation, angiogenesis and the production of new caverns are taking place in the “honeycombed” regions, which may result from signals caused by particular blood degradation products from hemorrhage and/or inflammatory cell infiltration into those areas. We propose that the foregoing processes are not occurring within the “bland” regions, which reflect mature quiescent areas that may have originally arisen from the “honeycombed” regions. It would be important to correlate MR relaxation times with clinical evidence of recent bleeding or CCM growth and with more detailed immunochemical observations of angiogenic activity and inflammation in different regions of the same lesion (1).

Although largely descriptive, these observations represent the first detailed images of CCM angioarchitecture at high field MR field strength. The technical possibilities and preliminary observations reported in the present work are anticipated to have importance as background for future mechanistic studies.

Acknowledgements

This research was supported in part by Grant K24NS02153 (IAA) and Grant S10RR019920 (AMW) from the National Institutes of Health and by Pilot and Career Development Grants (IAA) from Evanston Northwestern Healthcare Research Institute.

References

1. Abe M, Fukudome K, Sugita Y, Oishi T, Tabuchi K, Kawano T. Thrombus and encapsulated hematoma in cerebral cavernous malformations. Acta Neuropathol (Berl) 2005;109:503–509. [PubMed: 15759126]
2. Beall DP, Bell JP, Webb JR, Fish JR. Developmental venous anomalies and cavernous angiomas: a review of the concurrence, imaging, and treatment of these vascular malformations. J Okla State Med Assoc 2005;98:535–538. [PubMed: 16379482]
3. Blamire AM, Rowe JG, Styles P, McDonald B. Optimising imaging parameters for post mortem MR imaging of the human brain. Acta Radiol 1999;40:593–597. [PubMed: 10598845]
4. Bradley WG Jr. MR appearance of hemorrhage in the brain. Radiology 1993;189:15–26. [PubMed: 8372185]
5. Brekke C, Morgan SC, Lowe AS, Meade TJ, Price J, Williams SC, Modo M. The in vitro effects of a bimodal contrast agent on cellular functions and relaxometry. NMR Biomed 2007;20:77–89. [PubMed: 16952123]
6. Bruner, JM.; Tien, RD.; McLendon, RE. Tumors of vascular origin. In: Bigner, DD.; McLendon, RE.; Bruner, JM., editors. Russell and Rubinstein's Pathology of Tumors of the Nervous System. London: Arnold; 1998. p. 239-293.
7. Carr HY, Purcell EM. Effects of diffusion on free precession in nuclear magnetic resonance experiments. Phys Rev 1954;94:630–638.
8. Challa VR, Moody DM, Brown WR. Vascular malformations of the central nervous system. J Neuropathol Exp Neurol 1995;54:609–621. [PubMed: 7666048]
9. Chanda A, Nanda A. Multiple cavernomas of brain presenting with simultaneous hemorrhage in two lesions: a case report. Surg Neurol 2002;57:340–345. [PubMed: 12128311]
10. Clatterbuck RE, Eberhart CG, Crain BJ, Rigamonti D. Ultrastructural and immunocytochemical evidence that an incompetent blood-brain barrier is related to the pathophysiology of cavernous malformations. J Neurol Neurosurg Psychiatry 2001;71:188–192. [PubMed: 11459890]
11. Freeman R, Hill HDW. Fourier transform study of NMR spin-lattice relaxation by "progressive saturation". J Chem Phys 1971;54:3367–3377.
12. Gault J, Sarin H, Awadallah NA, Shenkar R, Awad IA. Pathobiology of human cerebrovascular malformations: basic mechanisms and clinical relevance. Neurosurgery 2004;55:1–17. [PubMed: 15214969]
13. Guclu B, Ozturk AK, Pricola KL, Bilguvar K, Shin D, O'Roak BJ, Gunel M. Mutations in apoptosis-related gene, PDCD10, cause cerebral cavernous malformation 3. Neurosurgery 2005;57:1008–1013. [PubMed: 16284570]
14. Jacobs RE, Ahrens ET, Dickinson ME, Laidlaw D. Towards a microMRI atlas of mouse development. Comput Med Imaging Graph 1999;23:15–24. [PubMed: 10091864]
15. Lehnhardt FG, von Smekal U, Ruckriem B, Stenzel W, Neveling M, Heiss WD, Jacobs AH. Value of gradient-echo magnetic resonance imaging in the diagnosis of familial cerebral cavernous malformation. Arch Neurol 2005;62:653–658. [PubMed: 15824268]
16. Margolis GOG, Woodhal B, Bloor BM. The role of small angiomatous malformations in the production of intracerebral hematomas. J Neurosurg 1951;8:564–575. [PubMed: 14889307]
17. Meiboom S, Gill D. Modified spin-echo method for measuring nuclear relaxation times. Rev Sci Instrum 1958;29:688–691.
18. Novak V, Chowdhary A, Abduljalil A, Novak P, Chakeres D. Venous cavernoma at 8 Tesla MRI. Magn Reson Imaging 2003;21:1087–1089. [PubMed: 14684215]

19. Otten P, Pizzolato GP, Rilliet B, Berney J. 131 cases of cavernous angioma (cavernomas) of the CNS, discovered by retrospective analysis of 24,535 autopsies [in French]. Neurochirurgie 1989;35:82–83. 128–131. [PubMed: 2674753]
20. Rigamonti D, Drayer BP, Johnson PC, Hadley MN, Zabramski J, Spetzler RF. The MRI appearance of cavernous malformations (angiomas). J Neurosurg 1987;67:518–524. [PubMed: 3655889]
21. Rigamonti D, Johnson PC, Spetzler RF, Hadley MN, Drayer BP. Cavernous malformations and capillary telangiectasia: a spectrum within a single pathological entity. Neurosurgery 1991;28:60–64. [PubMed: 1994283]
22. Robinson JR, Awad IA, Little JR. Natural history of the cavernous angioma. J Neurosurg 1991;75:709–714. [PubMed: 1919692]
23. Robinson JR Jr, Awad IA, Magdinec M, Paranandi L. Factors predisposing to clinical disability in patients with cavernous malformations of the brain. Neurosurgery 1993;32:730–736. [PubMed: 8492847]
24. Robinson JR Jr, Awad IA, Masaryk TJ, Estes ML. Pathological heterogeneity of angiographically occult vascular malformations of the brain. Neurosurgery 1993;33:547–555. [PubMed: 8232794]
25. Robinson JR Jr, Awad IA, Zhou P, Barna BP, Estes ML. Expression of basement membrane and endothelial cell adhesion molecules in vascular malformations of the brain: preliminary observations and working hypothesis. Neurol Res 1995;17:49–58. [PubMed: 7746343]
26. Rothbart D, Awad IA, Lee J, Kim J, Harbaugh R, Criscuolo GR. Expression of angiogenic factors and structural proteins in central nervous system vascular malformations. Neurosurgery 1996;38:915–925. [PubMed: 8727816]
27. Shenkar R, Sarin H, Awadallah NA, Gault J, Kleinschmidt-DeMasters BK, Awad IA. Variations in structural protein expression and endothelial cell proliferation in relation to clinical manifestations of cerebral cavernous malformations. Neurosurgery 2005;56:343–354. [PubMed: 15670382]
28. Tovi M, Ericsson A. Measurements of T1 and T2 over time in formalin-fixed human whole-brain specimens. Acta Radiol 1992;33:400–404. [PubMed: 1389643]
29. Tu J, Stoodley MA, Morgan MK, Storer KP. Ultrastructural characteristics of hemorrhagic, nonhemorrhagic, and recurrent cavernous malformations. J Neurosurg 2005;103:903–909. [PubMed: 16304995]
30. Uranishi R, Awadallah NA, Ogunshola OO, Awad IA. Further study of CD31 protein and messenger ribonucleic acid expression in human cerebral vascular malformations. Neurosurgery 2002;50:110–116. [PubMed: 11844241]
31. Uranishi R, Baev NI, Kim JH, Awad IA. Vascular smooth muscle cell differentiation in human cerebral vascular malformations. Neurosurgery 2001;49:671–680. [PubMed: 11523679]
32. Uranishi R, Baev NI, Ng PY, Kim JH, Awad IA. Expression of endothelial cell angiogenesis receptors in human cerebrovascular malformations. Neurosurgery 2001;48:359–368. [PubMed: 11220380]
33. Wong JH, Awad IA, Kim JH. Ultrastructural pathological features of cerebrovascular malformations: a preliminary report. Neurosurgery 2000;46:1454–1459. [PubMed: 10834648]
34. Yasui T, Komiyama M, Iwai Y, Yamanaka K, Matsusaka Y, Morikawa T, Ishiguro T. A brainstem cavernoma demonstrating a dramatic, spontaneous decrease in size during follow-up: case report and review of the literature. Surg Neurol 2005;63:170–173. [PubMed: 15680664]
35. Yong-Hing CJ, Obenaus A, Stryker R, Tong K, Sarty GE. Magnetic resonance imaging and mathematical modeling of progressive formalin fixation of the human brain. Magn Reson Med 2005;54:324–332. [PubMed: 16032673]

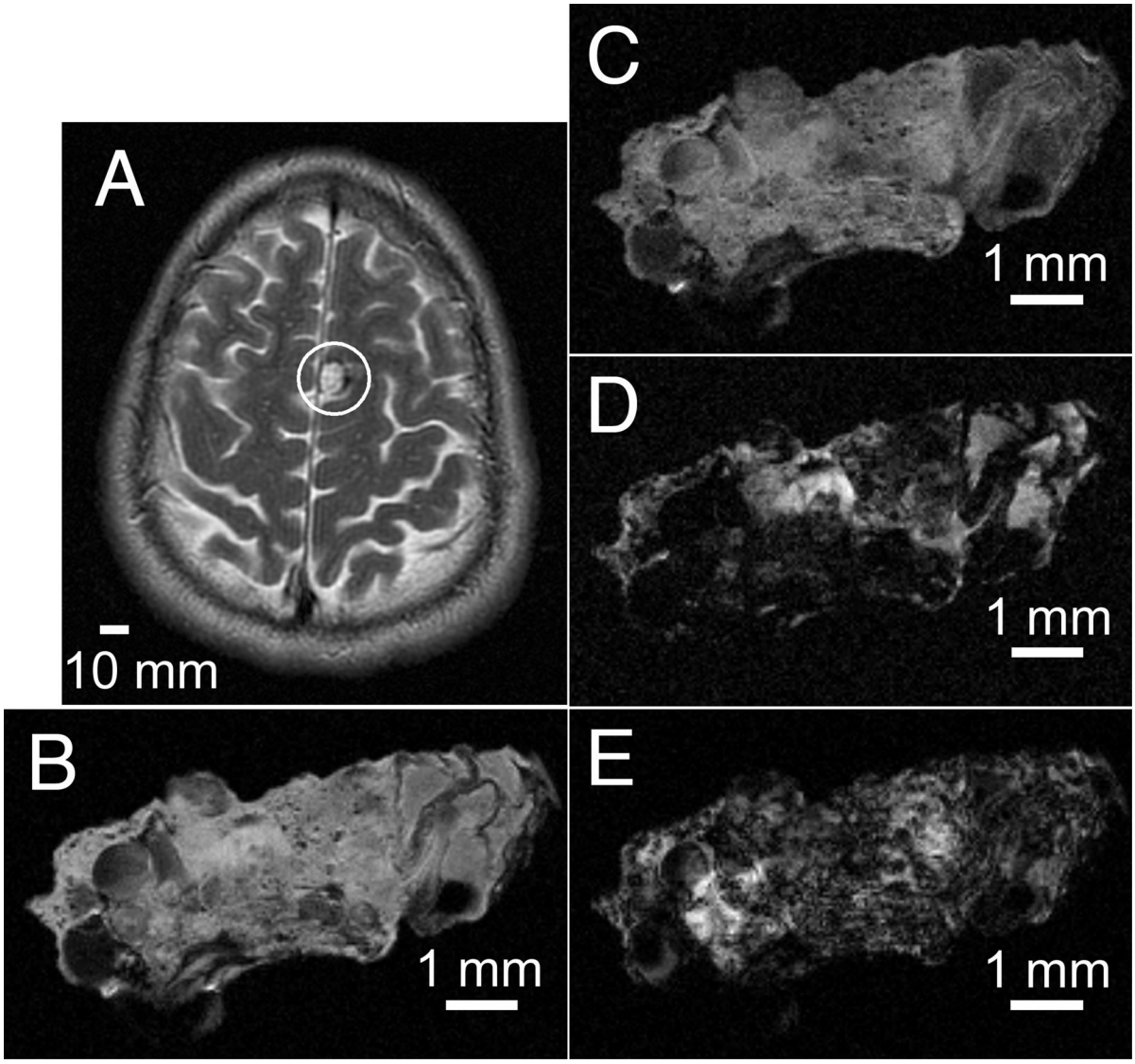

Figure 1.

In vivo and ex vivo MR images from a human CCM lesion. The indication for surgery was a presentation with new onset seizures, and the desire for the solitary lesion to be excised to prevent future sequelae, and to taper off anticonvulsants. T_2-weighted (A) spin-echo brain images were acquired at 1.5 T. MR images from a fragment of the same CCM lesion were acquired *ex vivo* following surgical excision on a 9.4 T microimager. (B) Spin-echo image with proton density contrast. (C) Spin-echo image with T_1-weighted contrast. (D) Spin-echo image with T_2-weighted contrast. (E) Gradient-recalled echo image with T_2*-weighted contrast. Slice thicknesses are 5 mm with a 1.5 mm gap (A) and 200 μm (B – E). Fields of view are 220 μm × 170 mm (A) and 10 mm (B – E). Matrix sizes are 256 × 224 (A) and 256 × 256 (B – E). Scale bars are 10 mm (A) and 1 mm (B – E).

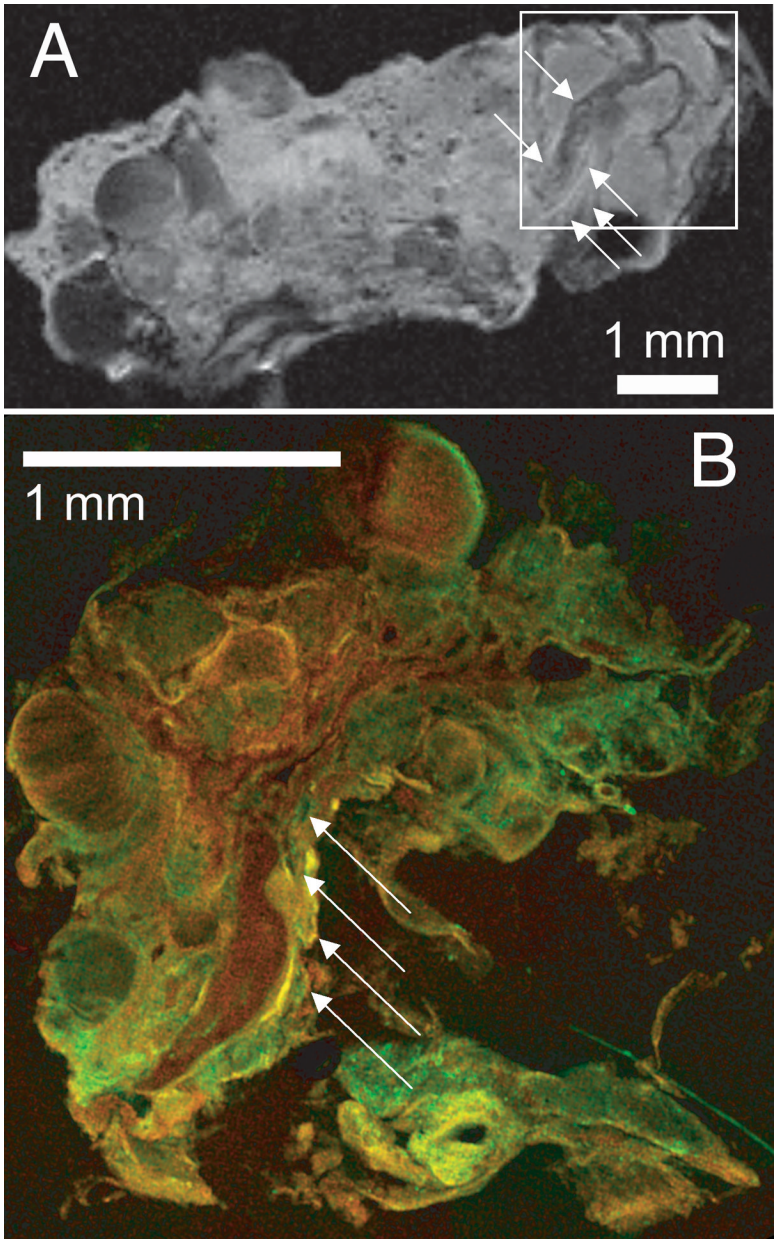

Figure 2.
Caverns along apparent blood vessels in proton density MR (A) and confocal microscope images (B) of CCM lesion *ex vivo*. The confocal histology image, from a region indicated by a square on the MR image of the same specimen, shows small caverns < 100 μm (arrows) along an apparent blood vessel. Slice thickness is 200 μm, field of view is 12 mm and matrix size is 256 × 256. Scale bars are 1 mm.

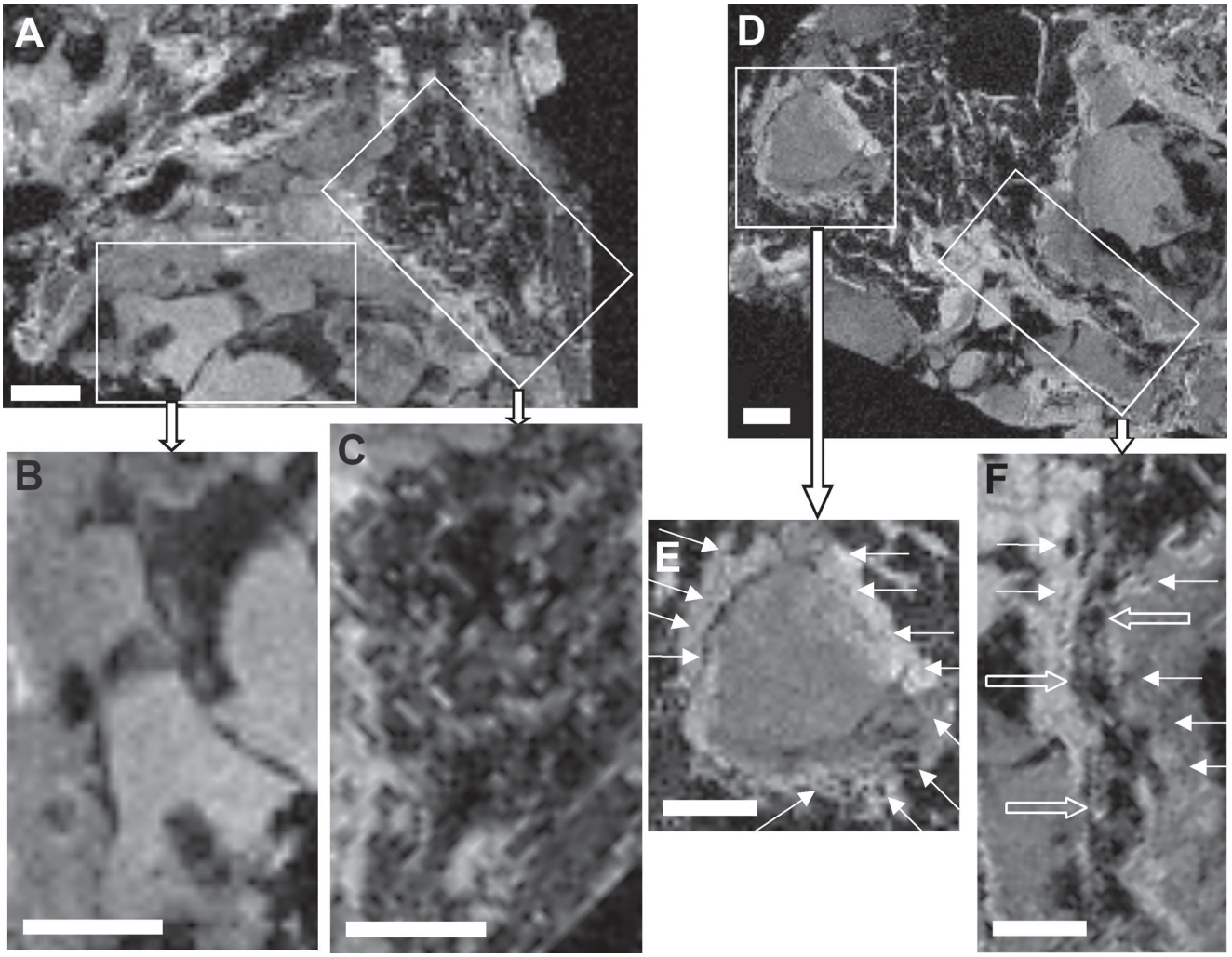

Figure 3.

Gradient-recalled echo T_2*-weighted MR images from a human CCM specimen acquired *ex vivo* on a 14.1 T microimager. Two enlarged views from a fragment of the lesion (A) showed large caverns with "bland" (B) and honeycombed (C) features in different regions. Two enlarged views from another fragment (D) showed small caverns < 100 μm (arrows) surrounding a larger cavern (E) and along an apparent blood vessel indicated by the open arrows (F). Slice thicknesses are 50 μm, fields of view are 15 × 15 × 13 mm and matrix sizes are 256 × 256 × 200. Scale bars are 1 mm.

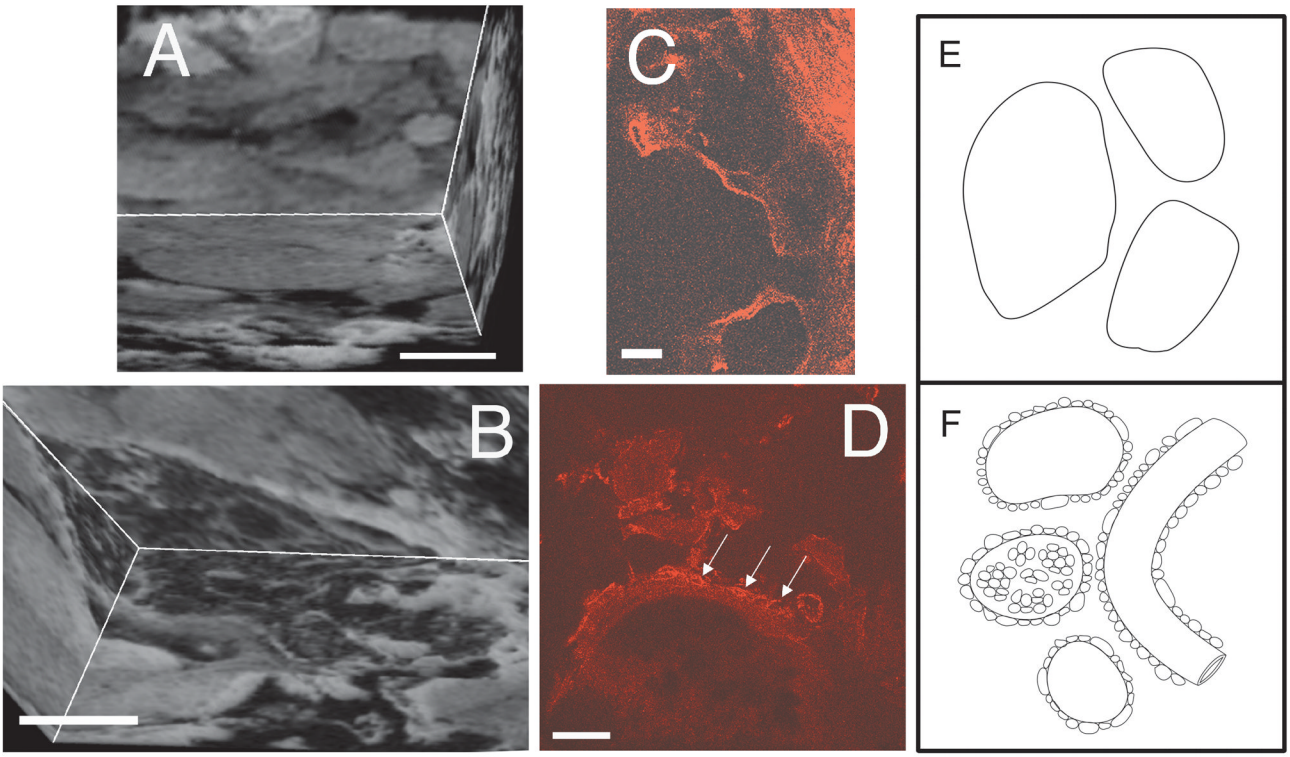

Figure 4.

Reconstructed three dimensional gradient-recalled echo T_2*-weighted MR images from a stack of serial two-dimensional images acquired *ex vivo* on a 14.1 T microimager (A, B), confocal images (C, D) and diagrams (E, F) showing “bland” (A, C, E) and “honeycombed” features (B, D, F) in the human CCM. Field of view is 15 × 15 × 13 mm; matrix size is 256 × 256 × 200 (A, B). The confocal sections were stained for von Willebrand factor (red). The scale bars are 500 μm (A, B) and 100 μm (C, D).

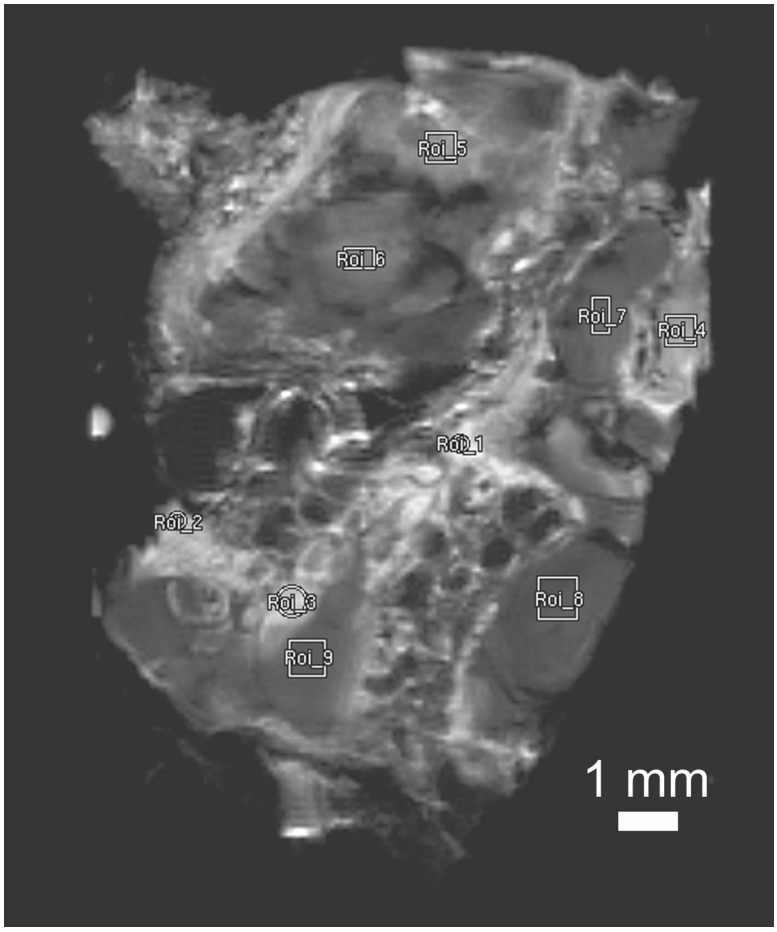

Figure 5.
Nine regions of interest for T_1 and T_2 relaxation time measurements shown in Table 1, selected on a proton-density weighted spin-echo image of CCM specimen from the third patient acquired *ex vivo* at 14.1 T. Slice thickness 500 μm, field of view 18 mm × 18 mm and matrix size 256 × 256 (in-plane pixel size 70 μm). Only regions with apparent signal intensity were selected for relaxation measurements. Curve fitting was not possible in regions that appear completely dark with no signal intensity.

TABLE 1

T_1 and T_2 relaxation times in a human CCM for regions of interest (ROI) indicated in Figure 5, obtained from MR at 14.1 T.

ROI	T_1	T_2
1	1.82 ± 0.26 s	34.95 ± 1.16 ms
2	1.69 ± 0.24 s	31.24 ± 0.85 ms
3	1.27 ± 0.11 s	30.07 ± 0.96 ms
4	1.43 ± 0.18 s	19.95 ± 0.81 ms
5	663.8 ± 52.5 ms	20.16 ± 1.00 ms
6	525.7 ± 42.8 ms	16.65 ± 1.20 ms
7	304.0 ± 16.7 ms	12.45 ± 1.36 ms
8	244.4 ± 10.3 ms	11.25 ± 2.08 ms
9	246.5 ± 12.2 ms	12.83 ± 1.67 ms